Microstructure and yield strength of SLM-fabricated CM247LC Ni-Superalloy

Wang, Xiqian; Carter, Luke N.; Pang, Bo; Attallah, Moataz M.; Loretto, Michael H.

DOI:
10.1016/j.actamat.2017.02.007

Document Version
Peer reviewed version

Citation for published version (Harvard):
Wang, X, Carter, LN, Pang, B, Attallah, MM & Loretto, MH 2017, 'Microstructure and yield strength of SLM-fabricated CM247LC Ni-Superalloy', *Acta Materialia*, vol. 128, pp. 87-95.
https://doi.org/10.1016/j.actamat.2017.02.007

Accepted Manuscript

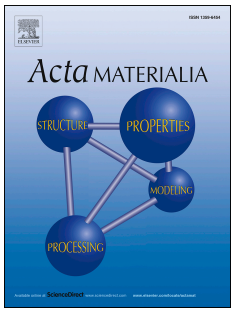

Microstructure and yield strength of SLM-fabricated CM247LC Ni-Superalloy

Xiqian Wang, Luke N. Carter, Bo Pang, Moataz M. Attallah, Michael H. Loretto

PII: S1359-6454(17)30098-8

DOI: 10.1016/j.actamat.2017.02.007

Reference: AM 13535

To appear in: *Acta Materialia*

Please cite this article as: Xiqian Wang, Luke N. Carter, Bo Pang, Moataz M. Attallah, Michael H. Loretto, Microstructure and yield strength of SLM-fabricated CM247LC Ni-Superalloy, *Acta Materialia* (2017), doi: 10.1016/j.actamat.2017.02.007

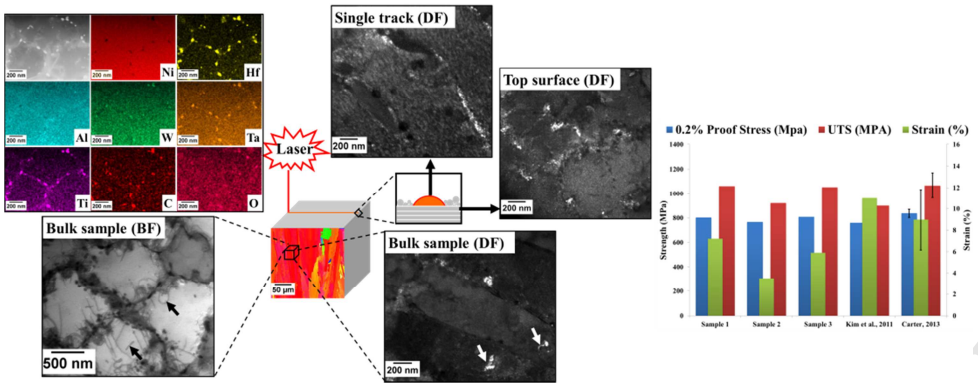

Microstructure and yield strength of SLM-fabricated CM247LC Ni-Superalloy

Xiqian Wang, Luke N. Carter, Bo Pang, Moataz M. Attallah and Michael H. Loretto*
Metallurgy and Materials, the University of Birmingham, Edgbaston, B15 2TT, UK

Abstract

Specimens of Selectively Laser Melted (SLM) CM247LC powder have been characterised using analytical scanning and transmission electron microscopy. In specimens from the bulk, it has been found that longitudinal sections consist mainly of columnar γ grains, containing virtually identically oriented cells, approximately 700 nm in width and length up to hundreds of microns. These cells are separated from adjacent cells and from adjacent grains by γ'/γ eutectic, by high densities of Hf/Ti/Ta/W-rich precipitates and high densities of dislocations. The eutectic γ' is up to about 50 nm in diameter but up to 10 nm within the cells. The microstructure in the top layer is similar to that taken from the bulk, but single-track samples are heterogeneous along the track length. The microstructures are interpreted in terms of the precipitation sequence, the volume fraction of eutectic and partitioning of the solute elements during solidification and the influence of subsequent laser-tracks. The cooling rate during solidification, calculated from the observed cell diameters is about 10^6 K/s, but the value obtained from the size of γ' within the bulk is about 10^4 K/s. It is suggested that the discrepancy is due to the limited accuracy of this approach. Tensile tests on as-fabricated samples show that the yield strength is comparable with that of cast samples after standard heat treatments. The high strength of the as-fabricated samples is interpreted in terms the high densities of precipitates and dislocations in cell boundaries, the fine cell structure and the γ' within cells.

Key words: Ni-base superalloys; Transmission Electron Microscopy; Selective laser melting; solidification microstructure; tensile behaviour.

1. Introduction

The significant advantages, in producing near-net shape components with short lead time and low wastage of materials, have driven research into the application of Selective Laser Melting (SLM) in many areas such as aero-engine components and medical implants [1, 2]. A considerable amount of work has been published on the response of a range of alloys to SLM [3-5] and a great deal of work has been carried out aimed at optimising the process conditions to minimise the density of pores and cracks formed during SLM. Studies have also shown that both cracks and pores can be further minimised by post-process Hot Isostatic Pressing (HIPping) [6-8].

In Ni-base superalloys, the precipitation of large amounts of γ' provides precipitation hardening and excellent high-temperature mechanical properties [9-11]. Radis *et al.* [9] reported that the higher cooling rate during continuous cooling of UDIMET 720 Li from above the solution temperature, gives finer γ' precipitates, which are more spherical and are of uniform size. In a similar study carried out on the CM247DS alloy [12], it was found that water-quenched (~10^3 K/s) samples show a much higher density, finer size (~40 nm), more spherical and a more uniform distribution of γ' precipitates than those in samples cooled at 75 K/s. Kusabiraki *et al.* [13] reported that the effective cooling rate to avoid the precipitation of γ' in Nimonic 105 needs to be higher than 10^4 K/s.

In the case of high γ'-fraction Ni-base superalloys processed by SLM (e.g. CM247LC), where it is accepted that the cooling rates are high, the occurrence of cracking is a dominant feature due to the high residual stresses that result from rapid cooling and the susceptibility of these alloys to various cracking mechanisms [14-18]. In contrast to comprehensive studies on SLM process-optimisation to reduce the cracks and pores observed in the builds, only a limited amount of work has been published on the

development of the microstructure in laser-processed materials. The work that has been published has focused on optical microscopy and scanning electron microscopy (SEM), although very recently, Divya *et al.* [4] used transmission electron microscopy (TEM) to investigate the microstructure of CM247LC formed during SLM processing, but their interpretation of the observed microstructures differs from that in the present paper. There is also a lack of information concerning the cooling rates and data on the size and distribution of γ' precipitates in SLM-processed CM247LC, although several studies suggest cooling rates $>10^5$ K/s [19, 20]. Since precipitates, in the as-fabricated condition, can range in size down to a few nm [21], characterisation of the structures requires TEM. Earlier studies have related the primary Dendrite Arm Spacing (DAS) λ_1 (equivalent to cell spacing) to the cooling rate ($\dot{T}$) experimentally and theoretically, deriving Eq.1 [22]. Harrison *et al.* found $|\dot{T}| \sim 3\times10^5$ K/s with primary DAS of 0.9~1.2 μm during SLM of Hastelloy X [1].

$$\lambda 1 = 97(\pm 5)\dot{T}^{-0.36(\pm 0.01)} \quad (1)$$

The terminology, which will be used throughout this paper, will be explained, as was done in the recent paper [23] on AlSi10Mg, because different authors have used “cells” to describe different microstructures in SLM-processed samples. The terminology here will follow that used to describe the microstructures developed during solidification of alloys at different cooling rates [24]. These cells are similar to dendrites with effectively no secondary arms (very short secondary arms may well be formed) that grow into the liquid, forming an array of parallel cells of the same orientation if they originate from the same nucleus. Grain boundaries are formed when groups of cells growing from different nuclei meet.

The aim of this investigation is to characterise the microstructure and tensile properties of SLM-processed CM247LC by carrying out a detailed assessment of the microstructure in SLM-processed samples. This work has allowed the cooling rates occurring during solidification to be estimated through measurement of the cell width (equivalent to primary dendrite arm spacing) and the cooling rate in the solid (below the γ'-solvus) by measurement of the γ'-size in Jominy end-quenched samples, in samples that were water quenched with a thermocouple insert and in as-fabricated samples. The yield strength of these as-fabricated samples have been measured and compared with cast and heat treated CM247LC [25].

2. Experimental

The CM247LC argon gas atomised powder (+15-53 µm), the composition (wt%) of which is listed in Table 1 was supplied by LPW Technology Ltd. (UK). Samples were fabricated using a 'Concept Laser M2 Laser powder Bed' machine [7], with a laser power of 150 W, a scan speed of 1500 mm/s, dimensionless scan spacing factor, (scan spacing (µm) / laser track width (µm)) of 0.3 and island scanning strategy with an island size of 5 mm. The track width is assumed to be 150 µm. These conditions selectively melt successive 20 µm thick layers of powder.

Table 1. the chemical composition of supplied powder (wt%).

Cr	Co	Mo	W	Ta	Ti	Al	Hf	C	B	Zr	Ni
8.31	9.15	0.54	9.4	3.2	0.73	5.62	1.28	0.07	0.02	0.01	Bal.

To assess the role of cooling rate on the size of γ', Jominy end quenching tests [26, 27] have been carried out on samples with dimensions according to [26]. The test bar was heated up to a solution treatment temperature of 1533 K and held for 2 h before quenching. The Jominy quenching apparatus directs a water column to quench the end of the test bar. The very end of the test bar (<500 µm distance from surface) was

prepared for TEM observation. Water quenching of a 10 mm cubic sample with an embedded K-type thermocouple, with an acquisition rate of 100 Hz, was also performed to measure the actual cooling rate. Measurements, of the size of γ', was used to assess the cooling rate below the γ'-solvus in SLM-processed samples.

Metallographic samples were prepared for both the longitudinal and transverse planes by sectioning both along the building direction (Z) and the laser-scanning plane. Samples, which were ground and polished to 0.05µm oxide suspension finish, were observed using a Philips XL-30 SEM operated at 20 KV to obtain Electron Back Scatter Diffraction (EBSD) maps and a JEOL 7000 operated at 20 KV to acquire secondary and backscattered electron (BSE) images. 3 mm diameter discs from longitudinal and transverse sections for TEM were spark eroded and ground down to 150 µm which were twin-jet electro-polished at -20 °C with a solution of 10% perchloric acid and 90% methanol using a Struers Tenupol-5 system.

Since SLM is a layer-wise process, transverse samples were prepared both from the bulk of SLM-processed samples and from the uppermost surface layer in order to assess the influence of the repeated thermal cycles on the initial microstructure by comparing the as-solidified microstructure of the top layer with the remelted/reheated microstructure taken from the bulk samples. Since the microstructure of the top layer sample may result from remelting of tracks by adjacent laser tracks during processing, the microstructure of a single track sample has been characterised and compared with that in the top layer and bulk. A rectangular sample of CM247LC (20x20x5 mm) was built as a substrate, and single track (10 mm in length) was scanned across the top of substrate, which had been recoated with a layer of powder prior to the single laser track. The single-track specimen (with the substrate) was sectioned perpendicular to the laser

scanning direction followed by mounting, grinding and polishing. The cross section of single track is around 150 μm thick and FIB (Focused ion beam) thinning was used to extract a TEM sample (14 x14 μm) from the single-track sample.

A 200 kV JEOL TEM interfaced to an Energy Dispersive X-ray Spectroscopy (EDX) facility has been used for assessment of the orientation relationships between cells and for assessment of the detailed microstructures. Diffraction patterns were taken either using an aperture and a defocused electron beam to define the area selected (selected area diffraction S.A.D.) when high angular resolution patterns were required, or using a small focused probe when the area had to be accurately defined (micro-diffraction patterns), to determine the orientations of adjacent cells. Some EDX analyses were carried out in the JEOL 2100, using a focused probe on selected areas.

A TALOS Scanning Transmission Electron Microscopy (STEM) operating at 200 kV has also been used to carry out microstructural assessment and to obtain X-ray maps to assess the compositions of the precipitates and to measure the extent of segregation to cell and grain boundaries. To complement X-ray maps, the probe was focused on specific areas for longer counting times than are used when obtaining X-ray maps in order to obtain more accurate local data. Measurements of the size of γ' precipitates in bulk, top layer and single track samples, used to estimate cooling rates below the γ' solvus, were carried out using 'feret' in ImageJ software where all precipitates are considered to be spherical of diameter defined by the largest dimension. To avoid background noise, no attempt was made to measure precipitates smaller than 3 nm.

Tensile tests at room temperature were carried out by Westmoreland Mechanical Testing & Research, Ltd. on as-fabricated samples, according to ASTM E8-15a [28], to

allow comparison with the strength of cast and heat-treated CM247LC. Three tensile specimens were tested in the Z-direction.

3. Results

SEM images of longitudinal sections are shown in Figure 1 and as has been reported in many papers [7, 29-31], columnar grains are formed growing towards the melt pool along the Z-direction. In addition, random regions of equiaxed grains are visible. This variation in microstructure has been reported in many alloys processed by SLM and has been attributed to local differences in thermal history [7, 29] or microstructural inhomogeneities and/or evaporation and condensation during SLM processing [32]. The present study focuses on the columnar grains, which dominate the microstructure. Comparison of the EBSD map (Figure 1 (a)), the secondary electron image (Figure 1 (b)) and back scattered electron image (Figure 1 (c)) shows that within the columnar grains there are regions which contain a high density of precipitates which separate regions where the precipitate density is obviously lower.

Figure 1.

Longitudinal samples. Typical images are shown in Figure 2 (a) and (b). The dislocation density is higher in the regions where the precipitates are present. Micro-diffraction patterns show that these precipitates and the associated dislocations define the boundaries between cells which are approximately 700 nm in width and of virtually identical orientation.

Figure 2.

Grain boundaries are not obviously different from cell boundaries in TEM images, since both are associated with high densities of dislocations and precipitates, but can be distinguished from cell boundaries by using diffraction data. Micro-diffraction patterns

taken using a focused probe from either side of the boundary in Figure 3 (a) are shown in Figure 3 (b) and (c) which confirms that this is a high angle boundary separating cells labelled (b) and (c), but in the TEM image grain boundaries cannot always be distinguished from cell boundaries.

Figure 3.

X-ray mapping in Figure 4 suggests that Ni, Co and W contents are lower in the boundary regions than in cell centres. The Al, Hf and Ti contents are however higher at boundaries. Precipitates visible in Figure 2 and Figure 3 are Hf, W, Ti and Ta-rich and contain C and/or O. It is suggested that evaporation of Al occurs during processing, might form oxides [32], leading to oxygen pickup by Ti, W, Hf, and Ta. Consequently, there are precipitates rich in O. Al and Cr contents are higher along boundaries which is consistent with the presence of eutectic liquid.

Figure 4.

Diffraction patterns taken from anywhere in these longitudinal sections show superlattice reflections as seen in Figure 5 (d). Dark field images, taken using superlattice γ' reflections, show that γ'/γ eutectic is present along parts of the cell boundaries and very much finer γ' is present within cells, as shown in Figure 5 (a). Some regions of eutectic γ' are not confined to cell boundaries although they are commonly contiguous with the eutectic in the cell boundaries in Figure 5 (b,c).

Figure 5.

It is clear from Figure 5 and from the bright field images shown in Figure 2 and Figure 3 that the cells in the longitudinal section are elongated in the Z-direction as would be expected from the SEM images and that the larger precipitates are far more frequent in the boundaries than within the cells. The γ'-fraction was determined to be ~1.5 vol%

from a series of dark field images taken in the eutectic regions, using a γ' reflection along the length of many long cells.

Transverse samples. TEM images of cross sections of the cells and boundaries, are shown in Figure 6 (a) and (b). The cells contain a significant dislocation density, although the density is far higher in the cell boundaries.

Figure 6.

STEM images (see Figure 7) taken on the Talos, both in bright field and using the high angle dark field detector show the microstructure more clearly than can be seen in TEM images. Dislocations within the cells and in cell boundaries are visible in both images and many are paired.

Figure 7

X-ray maps of transverse sections using the TALOS analytical STEM, are consistent with the maps from longitudinal sections as shown in Figure 8 showing that W content is also higher in the centres than in the boundaries, whereas the Ti, Al, Hf and Cr contents are higher in boundaries. When point counts are used, with longer counting times, it is found that the Ta and Hf concentrations are also higher in cell boundaries and C and/or O can always be detected in the precipitates. EDX analysis in TEM of the centres of the cells shows that the Ni content is about 58 wt.%, whereas analyses of the boundaries vary from 58 to 54wt.%.

Figure 8.

Further information confirming the nature of the boundaries can be obtained by imaging in dark field using a γ' reflection as shown in Figure 9. It is clear from the diffraction pattern in Figure 9 (b) that superlattice maxima from γ' are visible and imaging using the 010 diffraction maximum visible in Figure 9 (a) shows γ' particles up to about

50 nm in size present in the boundaries, together with far smaller γ' within the centres. The larger particles in the boundaries are formed as the eutectic composition solidifies, whereas the γ' in the centres is formed in the solid state from the γ. The compositional changes measured in the TALOS, where Ni and W contents are higher in the cell centres and Al, Cr and Ti contents are higher in boundaries, reflect the partitioning of these elements during solidification either to γ (in cell centres) or to the eutectic liquid (in cell and grain boundaries). However, the formation of Hf, W, Ti and Ta-rich precipitates reduces the amount of these elements in solution in the cell boundaries.

Figure 9.

The size of γ' has been used to estimate the cooling rate during cooling below the γ' solvus. The γ' in cell boundaries is significantly larger than in cell centres, which is to be expected since the γ' in the eutectic forms during solidification (the eutectic temperature is about 1503K), whereas the γ' in cell centres forms in the solid-state by precipitating from the γ (the γ' solvus is about 1523 K). The fine γ' precipitates in cell centres, are below about 20 nm in diameter, although the majority are about 10 nm and below. The Jominy tests showed that γ' precipitates are around 50 nm in diameter. Similar results are also found in [9, 12] when CM247LC was water quenched. The cooling rate was measured during water-quenching of 10 mm cubes and a value of around 10^3 K/s was found, which is in the agreement with the literature [12]. Although the response time of the thermocouple limits the ability to measure cooling rates accurately it is considered that the overall measurement is not greatly in error.

The microstructures in samples taken from the top surface are similar to those seen in samples taken from the bulk. In single track it is quite clear that the sample is heterogeneous since some un-melted regions are present, presumably because the

transfer of energy to the powder varies in different regions. The areas selected using FIB were chosen to avoid un-melted regions. Examination of the small region thinned using FIB showed that the microstructure was not homogeneous even on this scale. Thus Figure 10 (a) shows cells, which are either elongated approximately towards the centre of laser track or are equiaxed. Figure 10 (b) and (c) are dark field images taken using the 100 reflection which show some regions of eutectic ($\gamma + \gamma'$), mostly in cell boundaries and some fine γ' precipitates most of which are below 10 nm in diameter in the body of the γ cells. Precipitates are still obvious at cell boundaries, but the compositional differences obtained using point EDX analyses shows the extent of partitioning between cell boundaries and cell centres is less obvious than in samples from the bulk or from the top layer. A limited number of dislocations is also visible.

Figure 10.

The sizes of γ' particles within cells and at cell boundaries have been measured in samples taken from the bulk, from the top surface and from the single-track samples and these measurements are summarised in Figure 11. The results are shown as %s within size ranges, below 10 nm, between 10 and 20 nm, between 20 and 30 nm and greater than 30 nm. The results for the bulk sample and for the top layer are virtually identical with the majority of particles below 10 nm and very few above 30 nm which come from the eutectic. The results for the single-track sample are quite different with a higher % of precipitates in the larger size ranges.

Figure 11.

The yield strength was measured and had an average of 792 MPa, which is marginally higher than cast CM247LC after standard heat treatments reported by Kim *et al.* [25]. The UTS of the as-fabricated samples is also higher than Kim's data, as shown in

Figure 12. The ductility was however limited, presumably in part because of the presence of cracks, which are known to be present in as-fabricated CM247LC. Sample 2 that showed the lowest ductility fractured outside the gauge length. As shown in Figure 12 the ductility has been improved after HIPping (which can heal some cracks [18, 33]), and heat treatment, although there is a large scatter.

Figure 12.

4. Discussion

The observations on the longitudinal sections show a microstructure dominated by columnar grains that contain virtually identical orientation cells (rather than dendrites). The boundaries between the cells contain a high density of dislocations and of Hf/W/Ti/Ta-rich precipitates and regions of (γ' + γ) eutectic which contains γ' particles up to about 50 nm in diameter. Within the cells there is a high density of smaller γ' particles, mostly below 10 nm in diameter. In addition, within these long cells there are some small volumes of the larger γ', although some are contiguous with cell boundary γ'/γ eutectic. The microstructures observed in transverse sections are, as expected from the longitudinal sections, made up of cross-sections of the long cells and the cell boundaries visible in the longitudinal sections.

These structures can be understood if it is assumed that the groups of similarly oriented cells visible in longitudinal sections grow from a common nucleus; these cells leaving a eutectic liquid between them, which solidify during SLM. This liquid contains a large fraction of the Hf/W/Ti/Ta-rich particles, which are then associated with the eutectic [34]. The regions of eutectic (γ +γ') found within γ cells (mostly contiguous with the cell boundary eutectic) would then originate from small volumes of eutectic liquid trapped on the solid/liquid interface during solidification. The dislocations formed

within the cells and at cell boundaries are generated by the high stresses occurring during SLM, which in the case of CM247LC leads to extensive cracking [32]. It is suggested that the higher dislocation density near to the cell boundaries, than that within the cells, arises because the Hf/W/Ti/Ta-rich precipitates and the γ'/γ eutectic act as barriers to glide of dislocations which therefore accumulate in these regions of high precipitate density. The blocking of dislocations may contribute to the extensive cracking observed in SLM-processed CM247LC since stresses generated during SLM will increase if they cannot be relieved by glide or climb of dislocation.

This interpretation of the microstructures in as-fabricated SLM-processed CM247LC differs from that put forward in the paper by Divya *et al*. [4], where it was suggested that the coarser γ' in boundaries is due to coarsening occurring in the solid state associated with "the higher internal energy at these locations". Our suggestion, that the γ' in grain and cell boundaries is formed via the eutectic transformation, but the γ' within the cells is formed during post-solidification cooling by precipitation from γ, seems able to explain the microstructure more satisfactorily. The γ' formed as a eutectic will thus be coarser than that formed via a solid-state transformation because diffusion will be faster. The local compositions in cell and grain boundaries are consistent with partitioning between liquid and solid during solidification if eutectic liquid is left in these boundaries.

In our recent SLM work [23] on AlSi10Mg, it was shown that Al (with very little Si in solution) forms cells which, in this near eutectic alloy, leads to the production of a high volume fraction of the Al-Si eutectic liquid which is formed mostly at cell (and grain) boundaries, but a significant amount is trapped at the liquid solid interface leading to sub cells within the long cells, delineated by regions of Al-Si eutectic. This

microstructure is consistent with the interpretation of the microstructure of SLM-processed CM247LC, with the only difference being that the volume fraction of eutectic is very much higher in the AlSi10Mg alloy so that the sub cell boundaries are a major feature in this alloy, whereas in CM247LC no obvious sub cell boundaries are seen and isolated regions of eutectic within cells are observed relatively rarely.

In addition to this difference in interpretation of the origin of the regions containing different sized γ' in SLM-processed CM247LC, there are some slight differences in the reported microstructures between the present work and that reported by Divya *et al*. [4]; they report a gradual change in orientation between adjacent cells whereas we find small, but not systematic changes. These differences could be associated with the different laser scanning strategies used and other variables during processing.

As noted above the data obtained in the present work allows two estimates of the cooling rate; firstly, the cooling rate during solidification from measurement of the cell size, (which is equivalent to primary dendrite arm spacing, using equation 1) and secondly, the cooling rate in the solid state, below the γ' solvus, calculated from the size of γ' within cells.

In the single track samples cells are generally elongated and it is clear, both from the literature and from the fact that the cells grow against the direction of maximum thermal gradient (heat flow) and therefore towards to the centre of melt-pools. As a sample is built, the bulk of the sample, together with substrate act as heat sinks and the influence of re-melting due to successive laser-tracks and layers during process promotes cell growth along the building direction. The equiaxed cells (cross section of elongated cells) are 700 nm in diameter and if this value is used in Equation 1 a cooling rate during solidification of about 10^6 K/s is obtained.

The measurements of the size of the γ', in samples taken either from the bulk, or from the top surface summarised in Figure 11, show that the vast majority of the γ' is below 10 nm and is in cell centres and a small % above 10 nm, contained in the γ/γ' eutectic. On the other hand the size distribution in the single-track samples does not show a peak at 10 nm and contains a significant % from 10 nm up to above 20 nm. The presence of these larger γ' may be due to the fact that the eutectic formed from the liquid, which solidifies at the solid/liquid interface remains on the top surface, rather than in cell boundaries. Thus, when the single layer is laid down it is likely that some liquid will solidify on the top surface (as well as in cell boundaries) which will be re-dissolved either when further layers are melted or by adjacent tracks in the top layer. On that basis the vast majority of the γ' formed in cells is between the smallest size that can be measured with any confidence, about 3 nm and 10 nm.

Since the samples from the top layer and from the bulk have very similar size distributions of γ', it appears that the effective cooling rates in these samples are very similar, despite the reheating which undoubtedly occurs. If the reheating leads to melting, this will dissolve any γ' and subsequent precipitation can occur only once the temperature has dropped below the γ' solvus. Hence the growth of γ' can occur only during this cooling, which apparently occurs at approximately the same rate throughout the sample. Any subsequent re-heating, to below the γ' solvus occurs so rapidly that there is no time for any growth of γ'. On that basis, the effective cooling rate, below the γ' solvus is constant throughout the build and the figure of 10 nm is an indication of this effective rate.

The size of the γ' in the end section of the Jominy samples and in the directly water-quenched sample is about 50 nm (where the measured cooling rate was about 10^3 K/s).

On that basis the effective cooling rate in the solid-state during SLM is certainly greater than 10^3 K/s. In the work by Babu *et al.* [12] it was also found that water quenching gives γ' particles up to a size of about 50 nm. Babu *et al.* [12] measured the size of γ' for a range of cooling rates and if their data is extrapolated linearly to higher cooling rates it appears that γ' of about 10 nm diameter would be formed at a cooling rate of about 10^4 K/s. This suggests that the effective cooling rate, during SLM below the temperature at which γ′ forms in the solid, is about 10^4 K/s. The discrepancy between the estimate of 10^6 K/s, obtained from the cell size, and the value of 10^4 K/s, obtained from the size of the γ', is far greater than would be expected. It is suggested that accuracies of either or both of the two estimates are poor because of the extrapolation involved.

The detailed thermal history during SLM has not yet been measured directly and the influence of various important parameters such as thermal conductivity of powders is being modelled in many laboratories in an attempt to assess actual cooling rates. Modelling of the conditions used here is underway and a paper will be submitted shortly. Kusabiraki *et al.* [13] concluded that the cooling rate required to prevent the precipitation of γ' in Nimonic 105 needs to be higher than 10^4 K/s; at this cooling rate they reported that they could see no superlattice maxima. There are several mistakes in the indexing of the diffraction patterns shown in Fig. 2 in their paper, although superlattice maxima can be seen at the lower cooling rates, but are not obvious in the diffraction pattern taken from a sample cooled at a rate which they calculate to be 10^4 K/s.

As noted above the difference in composition between the cell boundaries and cell centres observed in the present work shows that even the rapid cooling occurring during SLM there is time for significant partitioning of elements between the liquid and solid

phases, with eutectic liquid being formed at cell (and grain) boundaries between cells. The X-ray maps, (together with point analyses carried out for longer times than the dwell times when recording X-ray maps), show that Hf, Ta, Ti, Cr and Al partition to the liquid phase and that Ni, Co and W partition to the solid, with no segregation detectable for Mo. This partitioning is similar to that observed in cast MARM 247 [35] where Hf, Ta, Ti, and Al were found to segregate to the liquid, W and Co segregated to the solid, and Mo, Cr, and Ni did not segregate consistently. The cast alloy had significant differences in composition from the alloy studied here, such as a higher Al content and lower W content, but the partitioning is quite similar despite the difference in composition and cooling rates. The observed partitioning is thus consistent with the conclusion that eutectic ($\gamma + \gamma'$) is formed between the γ cells in SLM-processed samples of CM247LC during solidification, which gives rise to the coarser γ' in the cell boundaries than in the cell centres.

If EDX is used to detect this segregation, which is on a scale of less than the cell width of about 700 nm it is necessary to use thin samples to limit beam spreading. The high voltage available of 200kV and the small probe in a TEM also limits beam spreading. Harrison *et al.* [1] used EDX in an SEM (presumably operating at about 20kV) to assess the level of segregation to cell or grain boundaries in as-fabricated samples of Hastelloy, but found no detectable segregation. However, the spatial resolution of EDX analysis of bulk samples in an SEM is downgraded to between about 3 and 5 μm by beam spreading. It would thus be very difficult to detect segregation in their samples where the cell size is only about 1μm. The absence of segregation reported by Harrison *et al.* [1] must therefore be treated with some reservation.

The fact that the yield strength of as-fabricated CM247LC is similar to that of conventionally produced CM247LC is associated with the precipitates in the boundaries, the small cell size and the fine γ' in the cells. The cast samples after standard heat treatments have a coarser microstructure, but a higher fraction of γ′ particles; the higher fraction of γ′ apparently compensates for the lower strength of the coarse grained microstructure in the cast samples. The observation that dislocations are commonly seen in pairs (Figure 7(b)) in as-fabricated samples confirms that the γ' influences the motion of dislocations. This high strength of as-fabricated samples is important because it means that the strength of as-fabricated CM247LC is high enough for application without heat treatments. In fact heat treatments carried out at high enough temperatures to solution treat the samples results in recrystallisation [33] and elimination of cell boundaries, which would reduce the strength, but a higher density of γ′ which would increase the strength. The data in Figure 12 shows that these two effects compensate and that there is no obvious change in strength associated with HIPping although importantly the ductility is improved. The limited amount of γ′ formed during SLM means that the microstructure of the alloy is not stable and may change significantly during service, which in addition to the limited ductility suggests either that further heat treatments (which could be part of a HIP cycle) would be required or that the powder bed be heated so that cooling would be slowed down and γ′ growth could occur. It is possible that using a heated powder bed would significantly reduce the crack density but for rotating parts it is likely that HIP would be required. Further work to optimise the microstructure is required and it would be sensible to use an alloy that was not as prone to cracking as CM247LC.

5. Summary

TEM and STEM analyses of the microstructure in SLM-processed CM247LC have focused on the effects of the rapid cooling associated with SLM on the microstructure and tensile strength. Correlations with cooling experiments (Jominy quench bar) and single track builds were carried out, suggesting the following findings:

1. SLM processing of CM247LC leads to γ grains, which contain virtually identically oriented γ cells. These contain a high density of fine γ' precipitates and are separated from adjacent cells and from adjacent γ grains, by γ'/ γ eutectic and high densities of Hf/Ta/W/Ti-rich precipitates and high densities of dislocations.

2. The microstructure observed in single-track specimens is heterogeneous and consists of regions of un-melted powder, both equiaxed and elongated cells.

3. Cooling rates, obtained from the cell size and from the size of γ', differ by two orders of magnitude, suggesting that the extrapolation involved in obtaining these rates leads to significant errors.

4. Partitioning of elements during solidification to solid (γ) and the liquid phase is observed, resulting in significant composition differences between cell centres and cell and grain boundaries and to the formation of Hf/Ta/W/Ti-rich precipitates.

5. The complex heating/cooling cycles lead to large stresses, which cause extensive cracking and high dislocation densities, particularly in cell and grain boundaries.

6. It is suggested that the Ta/W/Hf/Ti-rich precipitates limit dislocation mobility and thus contribute to the build up of residual stresses during SLM.

7. As-fabricated CM247LC has a yield strength, which is comparable with cast CM247LC after standard heat treatments, because of the fine cell structure and fine γ’ within these cells; however, this microstructure may change during service.

Acknowledgements

XW would like to acknowledge the financial support of the Advanced Materials & Processing Laboratory (AMPLab) and the School of Metallurgy and Materials for her PhD scholarship. The authors acknowledge the support from the Centre for Electron Microscopy at the University of Birmingham.

References

[1] N.J. Harrison, I. Todd, K. Mumtaz. Reduction of micro-cracking in nickel superalloys processed by Selective Laser Melting: a fundamental alloy design approach, Acta Materialia 94 (2015) 59-68.
[2] A. Fukuda, M. Takemoto, T. Saito, S. Fujibayashi, M. Neo, D.K. Pattanayak, T. Matsushita, K. Sasaki, N. Nishida, T. Kokubo. Osteoinduction of porous Ti implants with a channel structure fabricated by selective laser melting, Acta Biomaterialia 7 (2011) 2327-2336.
[3] L. Thijs, K. Kempen, J.-P. Kruth, J. Van Humbeeck. Fine-structured aluminium products with controllable texture by selective laser melting of pre-alloyed AlSi10Mg powder, Acta Materialia 61 (2013) 1809-1819.
[4] V. Divya, R. Muñoz-Moreno, O. Messé, J. Barnard, S. Baker, T. Illston, H. Stone. Microstructure of selective laser melted CM247LC nickel-based superalloy and its evolution through heat treatment, Materials Characterization 114 (2016) 62-74.
[5] C. Qiu, C. Panwisawas, M. Ward, H.C. Basoalto, J.W. Brooks, M.M. Attallah. On the role of melt flow into the surface structure and porosity development during selective laser melting, Acta Materialia 96 (2015) 72-79.
[6] L. Rickenbacher, T. Etter, S. Hövel, K. Wegener. High temperature material properties of IN738LC processed by selective laser melting (SLM) technology, Rapid Prototyping Journal 19 (2013) 282-290.
[7] L.N. Carter, C. Martin, P.J. Withers, M.M. Attallah. The influence of the laser scan strategy on grain structure and cracking behaviour in SLM powder-bed fabricated nickel superalloy, Journal of Alloys and Compounds 615 (2014) 338-347.
[8] F. Wang. Mechanical property study on rapid additive layer manufacture Hastelloy® X alloy by selective laser melting technology, The International Journal of Advanced Manufacturing Technology 58 (2012) 545-551.
[9] R. Radis, M. Schaffer, M. Albu, G. Kothleitner, P. Pölt, E. Kozeschnik. Multimodal size distributions of γ′ precipitates during continuous cooling of UDIMET 720 Li, Acta Materialia 57 (2009) 5739-5747.
[10] R.C. Reed. The superalloys, Cambridge Univ. Press, 2006.
[11] F.I. Versnyder, M. Shank. The development of columnar grain and single crystal high temperature materials through directional solidification, Materials Science and Engineering 6 (1970) 213-247.
[12] S. Babu, M. Miller, J. Vitek, S. David. Characterization of the microstructure evolution in a nickel base superalloy during continuous cooling conditions, Acta Materialia 49 (2001) 4149-4160.
[13] K. Kusabiraki, X.-m. Zhang, T. Ooka. The growth of γ' precipitates in a 53Ni-20Co-15Cr superalloy, ISIJ international 35 (1995) 1115-1120.

[14] O. Ojo, N. Richards, M. Chaturvedi. Contribution of constitutional liquation of gamma prime precipitate to weld HAZ cracking of cast Inconel 738 superalloy, Scripta materialia 50 (2004) 641-646.
[15] O. Ojo, M. Chaturvedi. On the role of liquated γ′ precipitates in weld heat affected zone microfissuring of a nickel-based superalloy, Materials Science and Engineering: A 403 (2005) 77-86.
[16] R. Sidhu, O. Ojo, M. Chaturvedi. Microstructural response of directionally solidified René 80 superalloy to gas-tungsten arc welding, Metallurgical and Materials Transactions A 40 (2009) 150-162.
[17] M. Zhong, H. Sun, W. Liu, X. Zhu, J. He. Boundary liquation and interface cracking characterization in laser deposition of Inconel 738 on directionally solidified Ni-based superalloy, Scripta materialia 53 (2005) 159-164.
[18] L.N. Carter, M.M. Attallah, R.C. Reed. Laser powder bed fabrication of nickel-base superalloys: influence of parameters; characterisation, quantification and mitigation of cracking, Superalloys 2012, Seven Springs, PA, (2012) 577-586.
[19] L. Thijs, M.L.M. Sistiaga, R. Wauthle, Q. Xie, J.-P. Kruth, J. Van Humbeeck. Strong morphological and crystallographic texture and resulting yield strength anisotropy in selective laser melted tantalum, Acta Materialia 61 (2013) 4657-4668.
[20] S. Li, Q. Wei, Y. Shi, Z. Zhu, D. Zhang. Microstructure characteristics of inconel 625 superalloy manufactured by selective laser melting, Journal of Materials Science & Technology 31 (2015) 946-952.
[21] K. Amato, J. Hernandez, L. Murr, E. Martinez, S. Gaytan, P. Shindo, S. Collins. Comparison of microstructures and properties for a Ni-base superalloy (alloy 625) fabricated by electron beam melting, Journal of Materials Science Research 1 (2012) 3.
[22] H. Davies. The structures of rapidly quenched nickel-based superalloy ribbons Produced by melt spinning, Rapid Solidification Processing, Principles and Technologies.--II (1980) 153-164.
[23] J. Wu, X. Wang, W. Wang, M. Attallah, M. Loretto. Microstructure and strength of selectively laser melted AlSi10Mg, Acta Materialia 117 (2016) 311-320.
[24] W. Kurz, D. Fisher. Fundamentals of solidification, 1986, Trans Tech Publications, Switzerland.
[25] I. Kim, B. Choi, H. Hong, Y. Yoo, C. Jo. Anomalous deformation behavior and twin formation of Ni-base superalloys at the intermediate temperatures, Materials Science and Engineering: A 528 (2011) 7149-7155.
[26] D. Hu, A. Huang, A. Grégoire, X. Li, X. Wu, M. Loretto. Determining continuous cooling phase transformation behaviour in ti-46al-8nb using jominy end quenching, Mater Sci Forum. Vol. 29 (2005) 172-175.
[27] T.P. Gabb, D.G. Backman, D.Y. Wei, D.P. Mourer, D. Furrer, A. Garg, D.L. Ellis. γ'formation in a nickel-base disk superalloy, Superalloys 2000, Seven Springs, PA, (2000) 17-21.
[28] Standard Test Methods for Tension Testing of Metallic Materials. ASTM International, 2015.
[29] L. Thijs, F. Verhaeghe, T. Craeghs, J.V. Humbeeck, J.-P. Kruth. A study of the microstructural evolution during selective laser melting of Ti–6Al–4V, Acta Materialia 58 (2010) 3303-3312.
[30] T. Vilaro, C. Colin, J.-D. Bartout, L. Nazé, M. Sennour. Microstructural and mechanical approaches of the selective laser melting process applied to a nickel-base superalloy, Materials Science and Engineering: A 534 (2012) 446-451.

[31] I. Yadroitsev, P. Krakhmalev, I. Yadroitsava, S. Johansson, I. Smurov. Energy input effect on morphology and microstructure of selective laser melting single track from metallic powder, Journal of Materials Processing Technology 213 (2013) 606-613.
[32] Xiqian Wang, Noriko Read, Luke N. Carter, R. Mark Ward, M.M. Attallah. Defect formation and its mitigation in selective laser melting of high gamma prime ni-base superalloys, Superalloys 2016, Seven Springs, PA, (2016).
[33] L.N. Carter. Selective laser melting of nickel superalloys for high temperature applications, PhD thesis, University of Birmingham, 2013.
[34] J. Doherty, A. Giamei, B. Kear. The importance of grain boundary morphology and cohesion on intergranular strength, Canadian Metallurgical Quarterly 13 (1974) 229-236.
[35] K. Zeisler-Mashl, B. Pletka. Segregation during solidification in the MAR-M 247 system(of nickel-base superalloys), Superalloys 1992, (1992) 175-184.

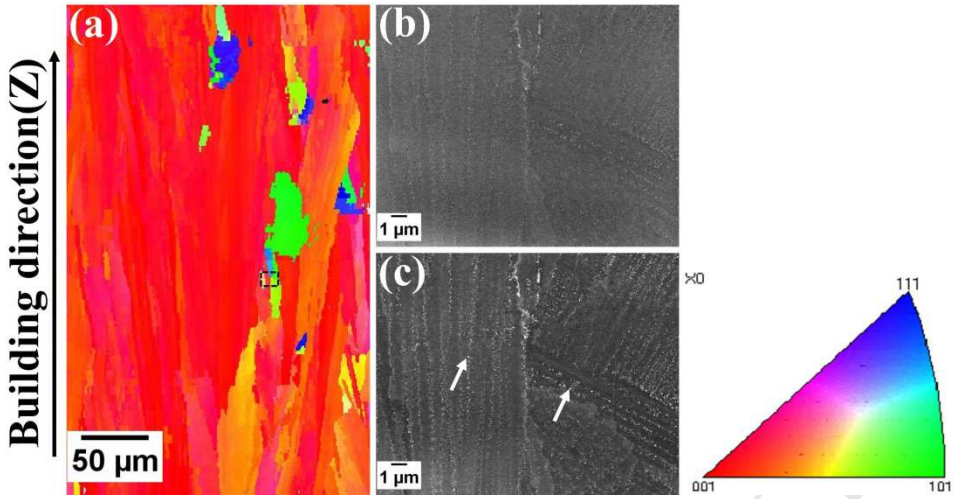

Figure 1. (a) EBSD map of as-fabricated sample showing strong <001> texture along the building direction; (b) a secondary electron image and (c) back scattered image (taken from area marked with dashed line in (a). High atomic number precipitates are bright and arrowed in (c).

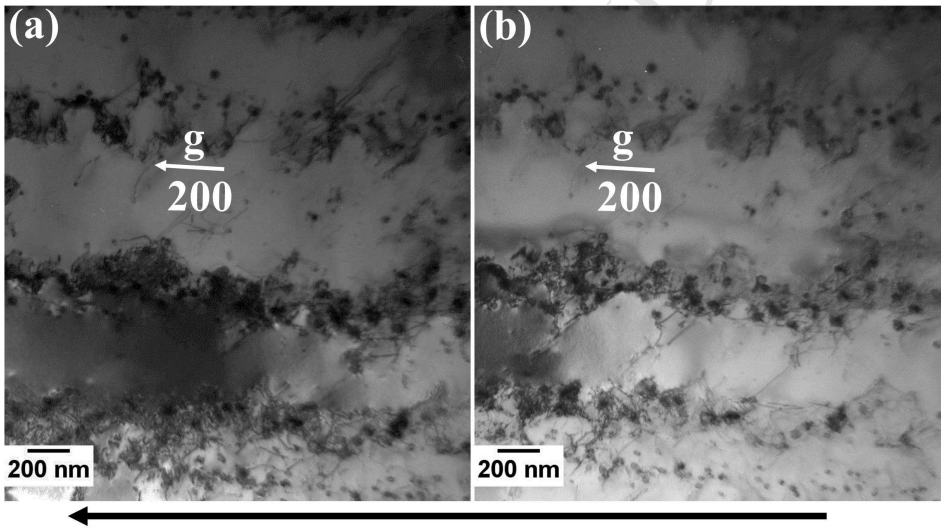

Figure 2. TEM bright field micrographs taken from longitudinal plane showing high densities of dislocations and precipitates imaged with g=200 (a) near the Bragg condition and (b) away from the Bragg condition. The building direction is marked underneath.

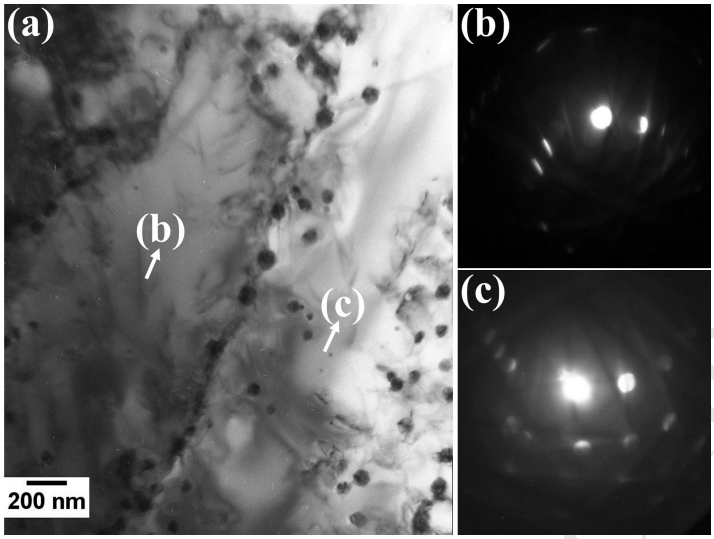

Figure 3. (a) Many beam TEM bright field micrograph of a boundary; (b) and (c) are micro-diffraction patterns taken from the arrowed areas in (a) which are of different orientations showing that the boundary between them is a high angle grain boundary.

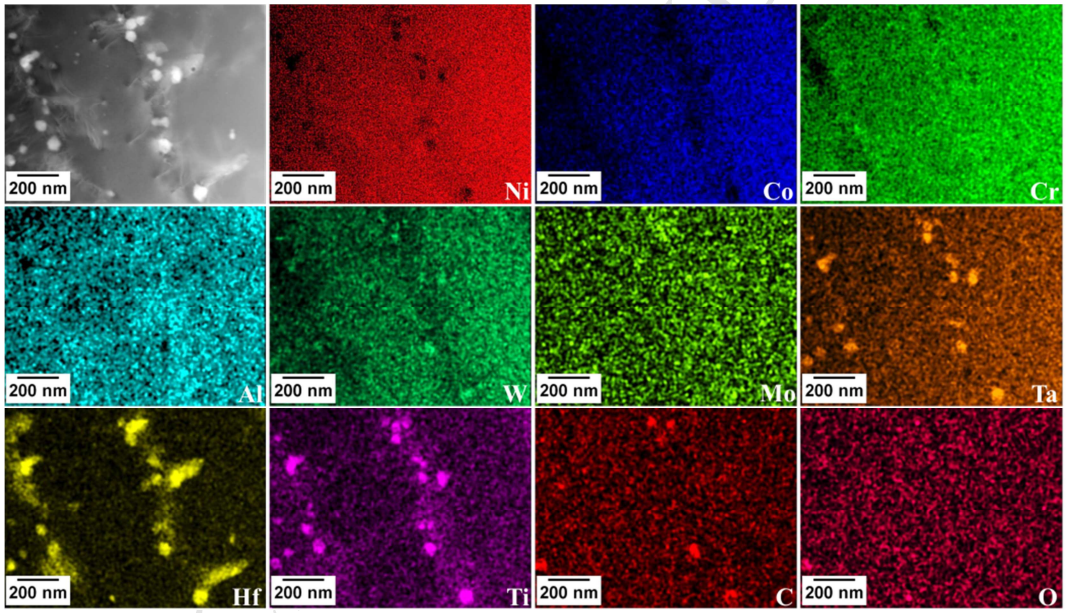

Figure 4. X-ray mapping of longitudinal section of an as-fabricated CM247LC TEM thin foil using the TALOS, showing higher Ni, Co and W contents within cells than at boundaries, while Al, Hf and Ti are higher in the cell boundaries; Hf, W, Ti and Ta-rich precipitates contain C and/or O.

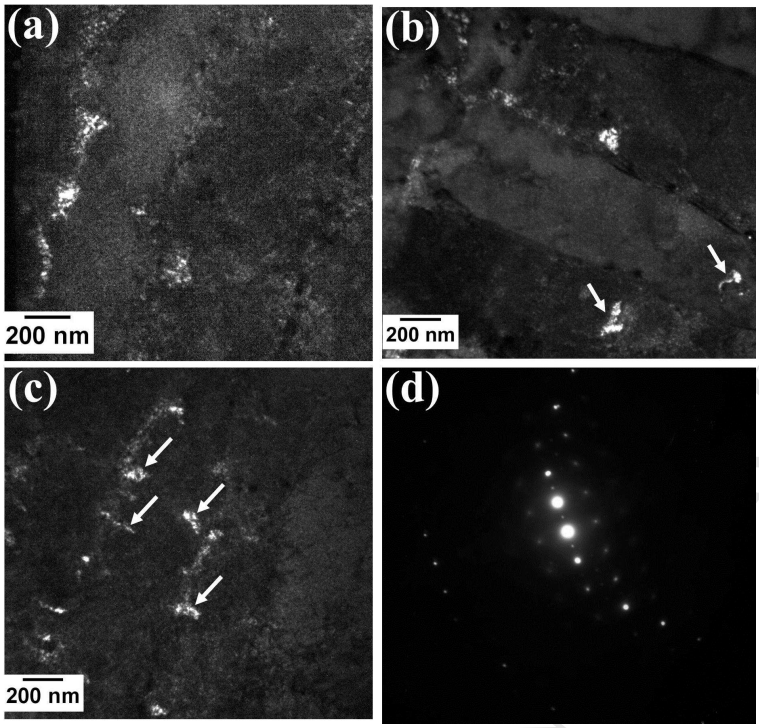

Figure 5. TEM dark field imaging from γ' reflections show in (a) γ'/γ eutectic containing relatively coarse γ' in parts of cell-boundaries and much finer γ' within cells; (b) and (c) some coarse γ'/γ eutectic (arrowed) is visible within cells, some of which is contiguous with the eutectic in the cell boundaries; (d) Selected area diffraction pattern taken close to a <100> beam direction, showing 010 superlattice reflections.

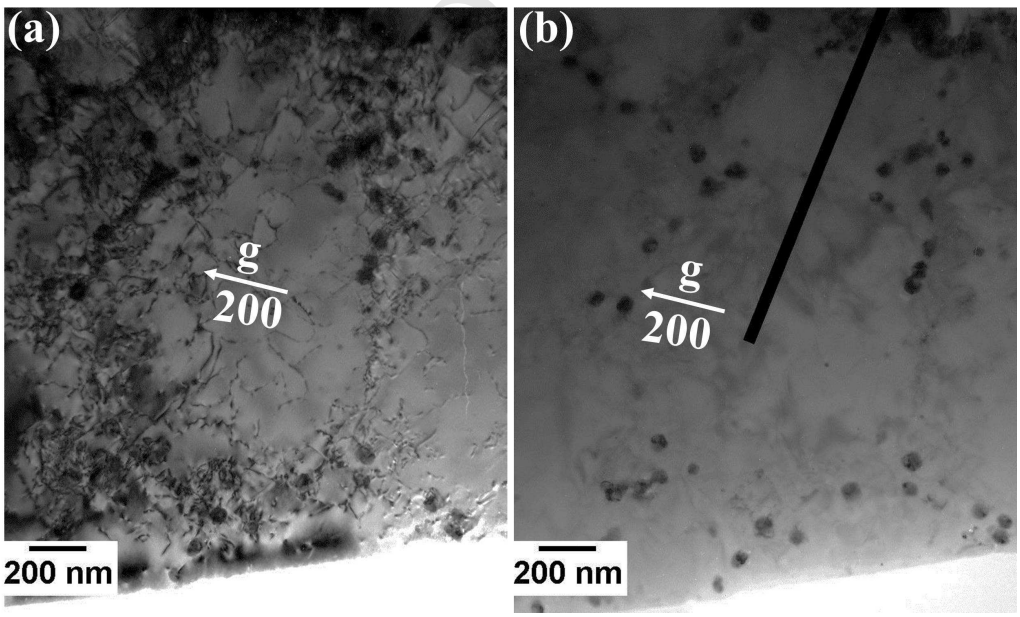

Figure 6. TEM bright field micrographs taken using g = 200 showing cross sections of cells imaged (a) near the Bragg, (b) away from the Bragg condition.

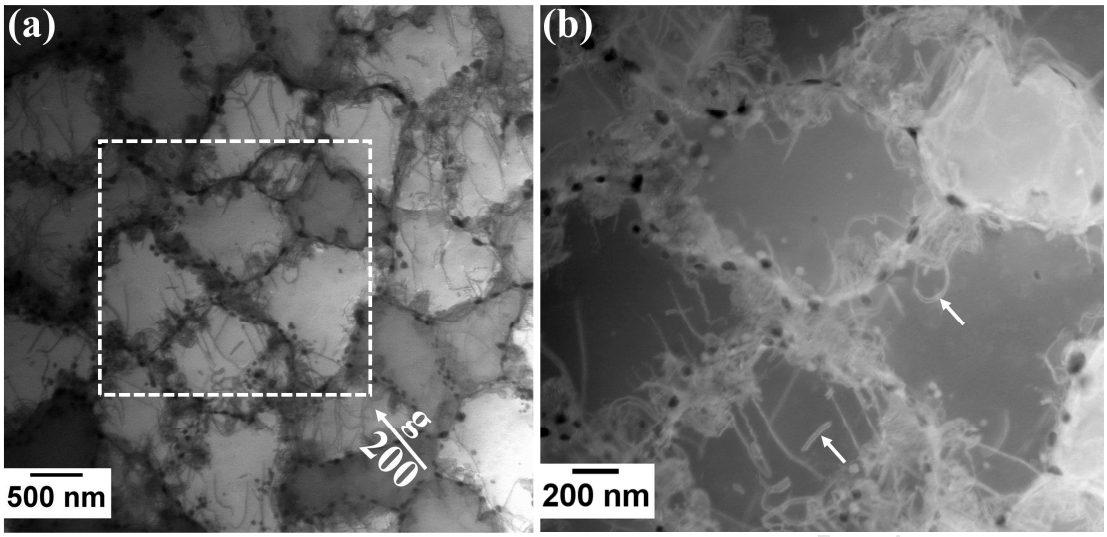

Figure 7. STEM images of transverse section of SLM-processed CM247LC (a) Bright field imaged using g = 200 (arrowed) and (b) corresponding HAADF image at higher magnification. Note paired dislocations (arrowed) visible in (b).

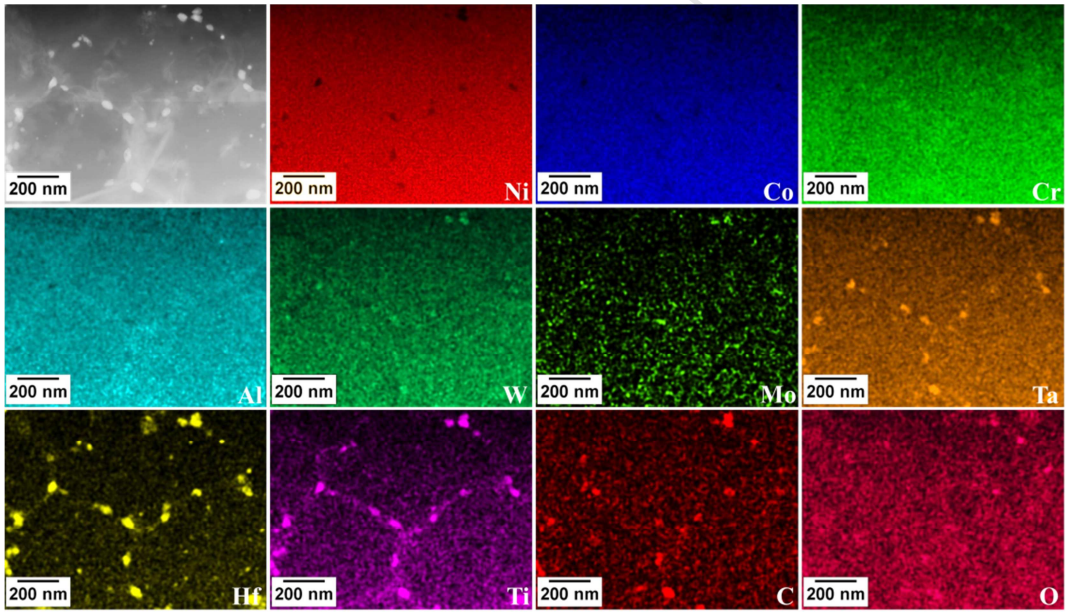

Figure 8. X-ray mapping of a transverse section of an as-fabricated CM247LC TEM foil using the TALOS showing higher W contents within cells than in cell boundaries, while Cr, Al, Hf and Ti contents are rich in the cell boundaries; Hf, Ti, W and Ta-rich precipitates contain C and/or O.

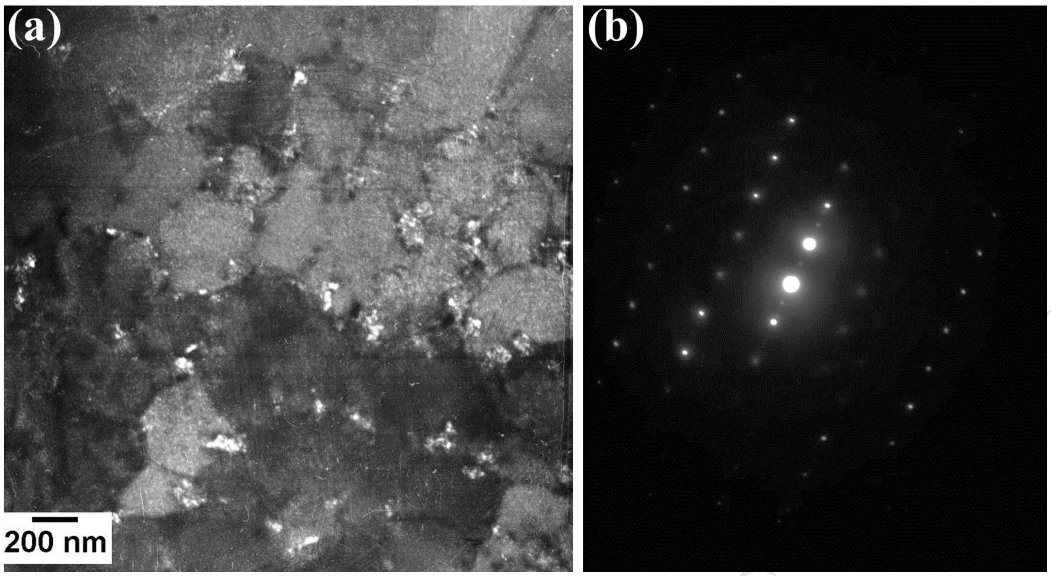

Figure 9. (a) TEM dark field imaging from γ' reflection shows γ'/ γ eutectic in cell boundaries, but much finer γ' is visible within cells; (b) selected area diffraction shows 020 fundamental and 010 superlattice reflections.

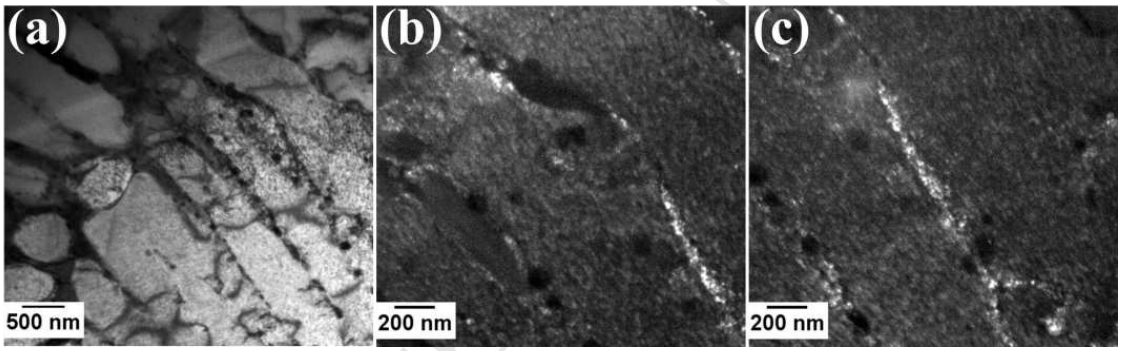

Figure 10. (a) TEM bright field image of single track sample revealing both elongated and equiaxed cells; (b, c) TEM dark field image taken with a γ' reflection showing γ /γ' eutectic at cell boundary and finer γ' (<10 nm in diameter) within cells; note the presence of precipitates, which are Hf/Ti/W/Ta-rich in cell boundaries.

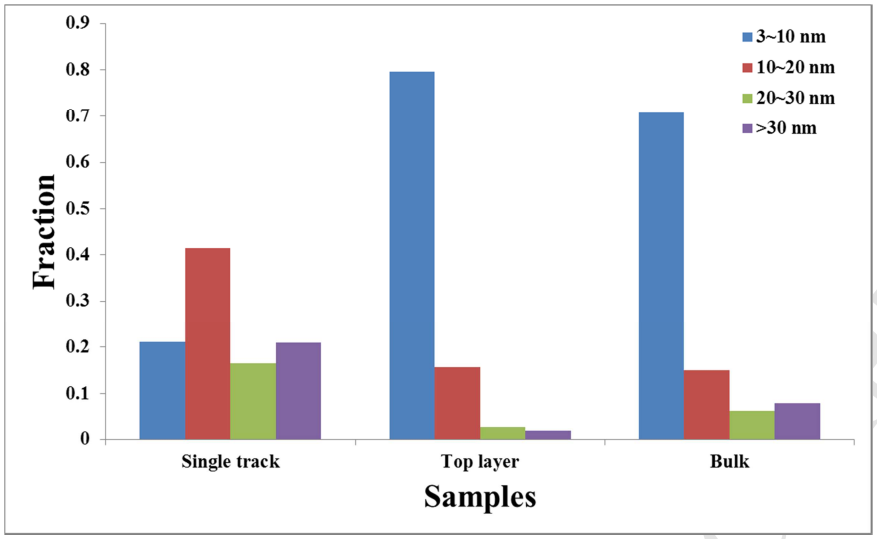

Figure 11. Showing the distribution of the size ranges of γ' particles within cells and in eutectic at cell boundaries taken from a single-track sample, from the top surface and from the bulk of SLM-processed samples of CM247LC.

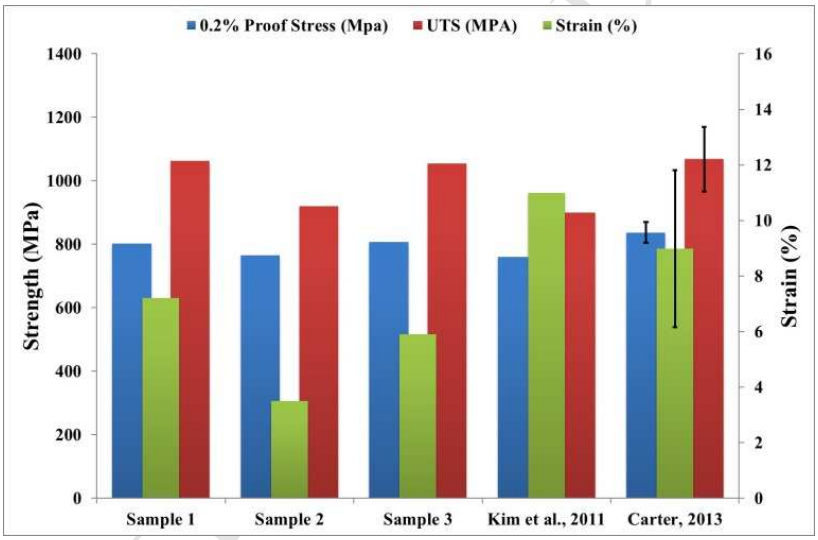

Figure 12. Bar plot showing the 0.2% proof stress, UTS and elongation at fracture of three as-fabricated CM247LC test samples, cast and heat treated CM247LC [27] and SLM of CM247LC after HIP and heat treatment [35].